

DiffFace: Blind Face Restoration with Diffused Error Contraction

Zongsheng Yue, Chen Change Loy
S-Lab

Nanyang Technological University

zsyzam@gmail.com, ccloy@ntu.edu.sg

Abstract

While deep learning-based methods for blind face restoration have achieved unprecedented success, they still suffer from two major limitations. First, most of them deteriorate when facing complex degradations out of their training data. Second, these methods require multiple constraints, e.g., fidelity, perceptual, and adversarial losses, which require laborious hyper-parameter tuning to stabilize and balance their influences. In this work, we propose a novel method named *DiffFace* that is capable of coping with unseen and complex degradations more gracefully without complicated loss designs. The key of our method is to establish a posterior distribution from the observed low-quality (LQ) image to its high-quality (HQ) counterpart. In particular, we design a transition distribution from the LQ image to the intermediate state of a pre-trained diffusion model and then gradually transmit from this intermediate state to the HQ target by recursively applying a pre-trained diffusion model. The transition distribution only relies on a restoration backbone that is trained with L_2 loss on some synthetic data, which favorably avoids the cumbersome training process in existing methods. Moreover, the transition distribution can contract the error of the restoration backbone and thus makes our method more robust to unknown degradations. Comprehensive experiments show that *DiffFace* is superior to current state-of-the-art methods, especially in cases with severe degradations. Code and model are available at <https://github.com/zsyOAOA/DiffFace>.

1. Introduction

Blind face restoration (BFR) aims at recovering a high-quality (HQ) image from its low-quality (LQ) counterpart, which usually suffers from complex degradations, such as noise, blurring, and downsampling. BFR is an extremely ill-posed inverse problem as multiple HQ solutions may exist for any given LQ image.

Approaches for BFR have been dominated by deep

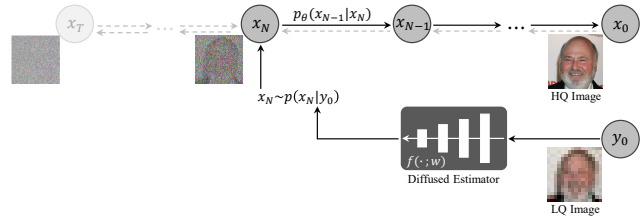


Figure 1. Overview of the proposed method. The solid lines denote the whole inference pipeline of our method. For ease of comparison, we also mark out the forward and reverse processes of the diffusion model by dotted lines.

learning-based methods [11, 14, 44, 45]. The main idea of them is to learn a mapping, usually parameterized as a deep neural network, from the LQ images to the HQ ones based on a large amount of pre-collected LQ/HQ image pairs. In most cases, these image pairs are synthesized by assuming a degradation model that often deviates from the real one. Most existing methods are sensitive to such a deviation and thus suffer a dramatic performance drop when encountering mismatched degradations in real scenarios.

Various constraints or priors have been designed to mitigate the influence of such a deviation and improve the restoration quality. The L_2 (or L_1) loss is commonly used to ensure fidelity, although these pixel-wise losses are known to favor the prediction of an average (or a median) over plausible solutions. Recent BFR methods also introduce the adversarial loss [12] and the perceptual loss [19, 51] to achieve more realistic results. Besides, some existing methods also exploit face-specific priors to further constrain the restored solution, e.g., face landmarks [5], facial components [24], and generative priors [3, 33, 45, 50, 52]. Considering so many constraints together makes the training unnecessarily complicated, often requiring laborious hyper-parameter tuning to make a trade-off among these constraints. Worse, the notorious instability of adversarial loss makes the training more challenging.

In this work, we devise a novel BFR method *DiffFace*, inspired by the recent success of diffusion model in image generation [7, 42]. Our method does not require multiple

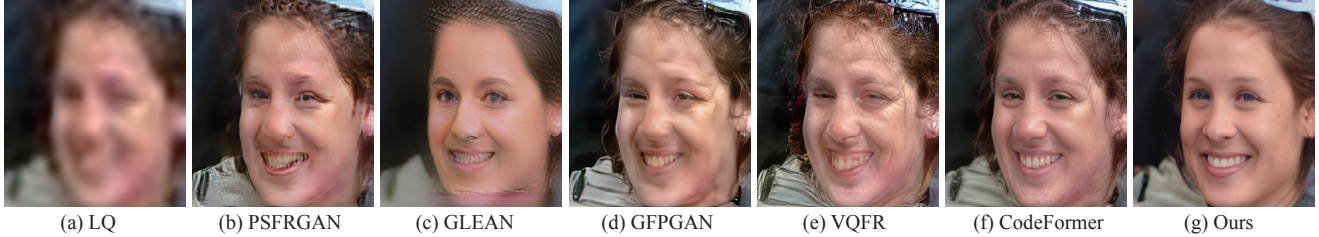


Figure 2. Comparative results with recent state-of-the-art methods on one typical real example. From left to right: (a) low-quality image, (b)-(g) restored results of GLEAN [3], PSFRGAN [4], GFPGAN [45], VQFR [14], CodeFormer [52], and our proposed method.

constraints in training, and yet is capable of dealing with unknown and complex degradations. Importantly, we leverage the rich image priors and strong generative capability of a pretrained diffusion model without retraining it on any manually assumed degradations.

To this end, we establish a posterior distribution $p(\mathbf{x}_0|\mathbf{y}_0)$, aiming to infer the HQ image \mathbf{x}_0 conditioned on its LQ counterpart \mathbf{y}_0 . Due to the complex degradations, solving for this posterior is non-trivial in blind restoration. Our solution to this problem, as depicted in Fig. 1, is to approximate this posterior distribution by a transition distribution $p(\mathbf{x}_N|\mathbf{y}_0)$, where \mathbf{x}_N is a diffused version of the desirable HQ image \mathbf{x}_0 , followed with a reverse Markov chain that estimates \mathbf{x}_0 from \mathbf{x}_N . The transition distribution $p(\mathbf{x}_N|\mathbf{y}_0)$ can be built up by introducing a neural network that is trained just using L_2 loss, and the reverse Markov chain is readily borrowed from a pretrained diffusion model containing abundant image priors.

The constructed transition distribution is appealing in that it is well motivated by an important observation in DDPM [16], where data is destroyed by re-scaling it with a factor of less than 1 and adding noise in the diffusion process. Bringing this notion to our context, the residual between \mathbf{x}_0 and \mathbf{y}_0 is also contracted by this factor after diffusion. Our framework uniquely leverages this property by inferring the intermediate diffused variable \mathbf{x}_N (where $N < T$) from the LQ image \mathbf{y}_0 , of which the residual to HQ image \mathbf{x}_0 is reduced. And then from this intermediate state we infer the desirable \mathbf{x}_0 . There are several advantages of doing so: i) our solution is more efficient than the full reverse diffusion process from \mathbf{x}_T to \mathbf{x}_0 , ii) we do not need to retrain the diffusion model from scratch, and iii) we can still take advantage of the pre-trained diffusion model via the reverse Markov chain from \mathbf{x}_N to \mathbf{x}_0 .

SR3 [38] also exploits the potentials of the diffusion model for blind restoration. It feeds the LQ image into the diffusion model as a condition to guide the restoration at each timestep. This requires one to retrain the diffusion model from scratch on pre-collected training data. Hence, it would still suffer from the issue of degradation mismatch when dealing with real-world data. Unlike SR3, our method does not need to train the diffusion model from scratch but

sufficiently leverages the prior knowledge of the pretrained diffusion model. The unique design on transition distribution $p(\mathbf{x}_N|\mathbf{y}_0)$ further allows us to better cope with unknown degradations.

In summary, the contributions of this work are as follows:

- We devise a new diffusion-based BFR approach to cope with severe and unknown degradations. Formulating the posterior distribution as a Markov chain that starts from the LQ image and ends at the desirable HQ image is novel. We show that the Markov chain can compress the predicted error by a factor of less than 1.
- We show that the image prior captured in a pretrained diffusion model can be harnessed by having the Markov chain built partially on the reverse diffusion process. Such a unique design also allows us to explicitly control the restoration’s fidelity and realism by changing the Markov chain’s length.
- We show that BFR can be achieved without complicated losses as in existing methods. Our method only needs to train a neural network with L_2 loss, simplifying the training pipeline. A preview of our results compared with existing methods is shown in Fig. 2.

2. Related Work

The BFR approaches mainly focused on exploring better face priors. We review a few popular priors in this section, including geometric priors, reference priors, and generative priors. Diffusion prior can be considered as a type of generative prior.

Geometric Priors. Face images are highly structured compared with natural images. The structural information, such as facial landmarks [5], face parsing maps [4, 4, 39], facial component heatmaps [24], and 3D shapes [17, 35, 53], can be used as a guidance to facilitate the restoration. The geometric face priors estimated from degraded inputs can be unreliable, affecting the performance of the subsequent BFR task.

Reference Priors. Some existing methods [8, 25] guide the restoration with an additional HQ reference image that owns the same identity as the degraded input. The main limitations of these methods stem from their dependence on the



Figure 3. Illustration of the diffused \mathbf{x}_N (top row) and the reconstructed results (bottom row) by a pretrained diffusion model from different starting timesteps. Note that the employed diffusion model is trained with 1000 discrete steps following [7].

HQ reference images, which are inaccessible in some scenarios. Li *et al.* [24] address this limitation by constructing an offline facial component dictionary based on the features extracted from HQ images. Then, it searches for the closest facial components in this dictionary for the given LQ images during restoration.

Generative Priors. Unlike [24], more recent approaches directly exploit the rich priors encapsulated in generative models for BFR. Following the paradigm of GAN inversion [48], the earliest explorations [13, 30, 33] iteratively optimize the latent code of a pretrained GAN for the desirable HQ target. To circumvent the time-consuming optimization, some studies [3, 45, 50] directly embed the decoder of the pre-trained StyleGAN [21] into the BFR network, and evidently improve the restoration performance. The success of VQGAN [10] in image generation also inspires several BFR methods. These methods mainly design different strategies, e.g., cross-attention [47], parallel decoder [14], and transformer [52], to improve the matching between the codebook elements of the degraded input and the underlying HQ image.

Attributed to the powerful generation capability of the diffusion model, some works based on diffusion model have been proposed recently. Typically, SR3 [38] and SRDiff [23] both feed the LQ image into the diffusion model as a condition to guide the restoration in training. To accelerate the inference speed, LDM [36] proposed to train the diffusion model in latent space of VQGAN [10]. These methods require one to retrain the diffusion model from scratch on some pre-collected data. The learned model would still be susceptible to the degradation mismatch when generalizing to other datasets. Therefore, this paper devises a new learning paradigm based on a pretrained diffusion model to address these issues.

3. Preliminaries

We provide a brief introduction to the diffusion probabilistic model [42] (known as diffusion model for brevity)

to ease the subsequent presentation of our method.

Diffusion model consists of a forward process (or diffusion process) and a reverse process. Given a data point \mathbf{x}_0 with probability distribution $q(\mathbf{x}_0)$, the forward process gradually destroys its data structure by repeated application of the following Markov diffusion kernel:

$$q(\mathbf{x}_t|\mathbf{x}_{t-1}) = \mathcal{N}(\mathbf{x}_t; \sqrt{1 - \beta_t}\mathbf{x}_{t-1}, \beta_t\mathbf{I}), \quad (1)$$

where $t \in \{1, 2, \dots, T\}$, $\{\beta_t\}_{t=1}^T$ is a pre-defined or learned noise variance schedule. With a rational design on the variance schedule, it theoretically guarantees that $q(\mathbf{x}_t)$ converges to the unit spherical Gaussian distribution. It is noteworthy that the marginal distribution at arbitrary timestep t has the following analytical form:

$$q(\mathbf{x}_t|\mathbf{x}_0) = \mathcal{N}(\mathbf{x}_t; \sqrt{\alpha_t}\mathbf{x}_0, (1 - \alpha_t)\mathbf{I}), \quad (2)$$

where $\alpha_t = \prod_{l=1}^t (1 - \beta_l)$.

As for the reverse process, it aims to learn a transition kernel from \mathbf{x}_t to \mathbf{x}_{t-1} , which is defined as the following Gaussian distribution:

$$p_\theta(\mathbf{x}_{t-1}|\mathbf{x}_t) = \mathcal{N}(\mathbf{x}_{t-1}; \boldsymbol{\mu}_\theta(\mathbf{x}_t, t), \boldsymbol{\Sigma}_\theta(\mathbf{x}_t, t)), \quad (3)$$

where θ is the learnable parameter. With such a learned transition kernel, we can approximate the data distribution $q(\mathbf{x}_0)$ via the following marginal distribution:

$$p_\theta(\mathbf{x}_0) = \int p(\mathbf{x}_T) \prod_{t=1}^T p_\theta(\mathbf{x}_{t-1}|\mathbf{x}_t) d\mathbf{x}_{1:T}, \quad (4)$$

where $p(\mathbf{x}_T) = \mathcal{N}(\mathbf{x}_T; \mathbf{0}, \mathbf{I})$.

4. Proposed Method

In this section, we present our BFR method that exploits the image priors encapsulated in a pretrained diffusion model. To keep the notations consistent with Sec. 3, we denote the LQ image and HQ image as \mathbf{y}_0 and \mathbf{x}_0 . To restore the HQ image from its degraded counterpart, we aim at designing a rational posterior distribution of $p(\mathbf{x}_0|\mathbf{y}_0)$.

4.1. Motivation

Considering a diffusion model with T discrete steps, it provides a transition function from \mathbf{x}_t to \mathbf{x}_{t-1} . With the aid of this transition, we can construct the posterior distribution $p(\mathbf{x}_0|\mathbf{y}_0)$ as follows:

$$p(\mathbf{x}_0|\mathbf{y}_0) = \int p(\mathbf{x}_N|\mathbf{y}_0) \prod_{t=1}^N p_\theta(\mathbf{x}_{t-1}|\mathbf{x}_t) d\mathbf{x}_{1:N}, \quad (5)$$

where $1 \leq N < T$ is an arbitrary timestep. Therefore, we can restore \mathbf{x}_0 from \mathbf{y}_0 by sampling from this posterior using ancestral sampling [1] from timestep N to 1 as follows:

$$\mathbf{x}_N \sim p(\mathbf{x}_N|\mathbf{y}_0), \quad \mathbf{x}_{t-1}|\mathbf{x}_t \sim p_\theta(\mathbf{x}_{t-1}|\mathbf{x}_t). \quad (6)$$

Since the transition kernel $p_\theta(\mathbf{x}_{t-1}|\mathbf{x}_t)$ can be readily borrowed from a pretrained diffusion model, our goal thus turns to design the transition distribution of $p(\mathbf{x}_N|\mathbf{y}_0)$.

We have an important observation by delving into Eq. (6). If replacing $p(\mathbf{x}_N|\mathbf{y}_0)$ with the marginal distribution $q(\mathbf{x}_N|\mathbf{x}_0)$ defined in Eq. (2), Eq. (6) degenerates into the diffusion and reconstruction process for \mathbf{x}_0 via a pretrained diffusion model, i.e.,

$$\underbrace{\mathbf{x}_N \sim q(\mathbf{x}_N|\mathbf{x}_0)}_{\text{Diffusion}}, \quad \underbrace{\mathbf{x}_{t-1}|\mathbf{x}_t \sim p_\theta(\mathbf{x}_{t-1}|\mathbf{x}_t)}_{\text{Reconstruction}}. \quad (7)$$

In Figure 3, we show some diffused and reconstructed results under different settings for the starting timestep N . One can observe that when N lies in a reasonable range (e.g., $N < 500$), meaning that \mathbf{x}_0 is slightly “destroyed”, it is possible to accurately reconstruct \mathbf{x}_0 using the pretrained diffusion model.

This observation indicates that $q(\mathbf{x}_N|\mathbf{x}_0)$ is an ideal choice for the desired $p(\mathbf{x}_N|\mathbf{y}_0)$ by setting a reasonable N . Since the HQ image \mathbf{x}_0 is inaccessible in the task of BFR, we thus explore how to design a plausible $p(\mathbf{x}_N|\mathbf{y}_0)$ to approximate $q(\mathbf{x}_N|\mathbf{x}_0)$.

4.2. Design

Recall that our goal is to design a transition distribution $p(\mathbf{x}_N|\mathbf{y}_0)$ to approximate $q(\mathbf{x}_N|\mathbf{x}_0)$. Fortunately, the target distribution $q(\mathbf{x}_N|\mathbf{x}_0)$ has an analytical form as shown in Eq. (2). This inspires us to formulate $p(\mathbf{x}_N|\mathbf{y}_0)$ as a Gaussian distribution as follows:

$$p(\mathbf{x}_N|\mathbf{y}_0) = \mathcal{N}(\mathbf{x}_N; \sqrt{\alpha_N}f(\mathbf{y}_0; w), (1 - \alpha_N)\mathbf{I}), \quad (8)$$

where $f(\cdot; w)$ is a neural network with parameter w , aiming to provide an initial prediction for \mathbf{x}_0 . It should be noted that the final restored result by our method is achieved by sampling from the whole Markov chain of Eq. (6) (see Fig. 1), and not directly predicted by $f(\cdot; w)$. As for $f(\cdot; w)$, it is only used to construct the marginal distribution of \mathbf{x}_N ,

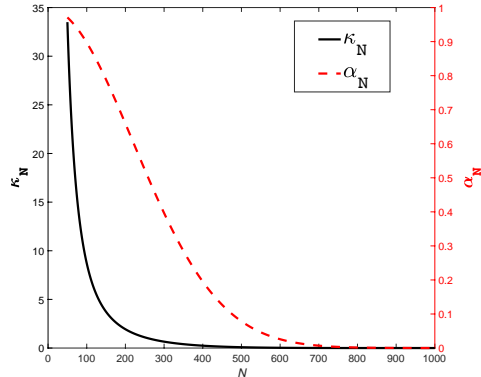


Figure 4. The curves of κ_N and α_N with the starting timestep N .

a diffused version of \mathbf{x}_0 , and thus named as “diffused estimator” in this work.

Next, we consider the Kullback-Leibler (KL) divergence between the designed $p(\mathbf{x}_N|\mathbf{y}_0)$ and its target $q(\mathbf{x}_N|\mathbf{x}_0)$. By denoting the predicted error of $f(\cdot; w)$ as $e = \mathbf{x}_0 - f(\mathbf{y}_0; w)$, we have

$$D_{\text{KL}} [p(\mathbf{x}_N|\mathbf{y}_0)||q(\mathbf{x}_N|\mathbf{x}_0)] = \frac{1}{2} \kappa_N \|e\|_2^2, \quad (9)$$

where $\kappa_N = \frac{\alpha_N}{1 - \alpha_N}$. As shown in Fig. 4, κ_N strictly decreases monotonically with the timestep N . Hence, larger N will offer a better approximation to $q(\mathbf{x}_N|\mathbf{x}_0)$, and further achieve a more realistic image via the designed posterior distribution of Eq. (5). However, \mathbf{x}_N will contain more noises when N is getting larger, as shown in Fig. 3. Thus, an overly large N will inevitably deviate the restored result from the ground truth \mathbf{x}_0 . Therefore, the choice of N induces a realism-fidelity trade-off for the restored HQ image. We provide the ablation study in Sec. 5.

4.3. Discussion

Instead of directly learning a mapping from \mathbf{y}_0 to \mathbf{x}_0 under multiple constraints like current deep learning-based methods [4, 45, 50], the proposed method circumvents this by predicting \mathbf{x}_N , a diffused version of \mathbf{x}_0 , from \mathbf{y}_0 . Such a new learning paradigm brings several significant advantages compared to existing approaches:

- **Error Contraction.** Considering the diffused estimator $f(\cdot; w)$, its predicted error is denoted as $e = \mathbf{x}_0 - f(\mathbf{y}_0; w)$. In our method, the problem of BFR is reformulated to predict \mathbf{x}_N as explained in Sec. 4.1. According to Eq. (8), \mathbf{x}_N can be accessed as follows:

$$\begin{aligned} \mathbf{x}_N &= \sqrt{\alpha_N}f(\mathbf{y}_0; w) + \sqrt{(1 - \alpha_N)}\zeta \\ &= \sqrt{\alpha_N}\mathbf{x}_0 - \sqrt{\alpha_N}e + \sqrt{(1 - \alpha_N)}\zeta, \end{aligned} \quad (10)$$

where $\zeta \sim \mathcal{N}(\zeta|\mathbf{0}, \mathbf{I})$. It can be seen that the predicted error e is contracted by a factor of $\sqrt{\alpha_N}$ under our proposed paradigm of predicting \mathbf{x}_N , where $\sqrt{\alpha_N}$ is less than 1 as shown in Fig. 4.

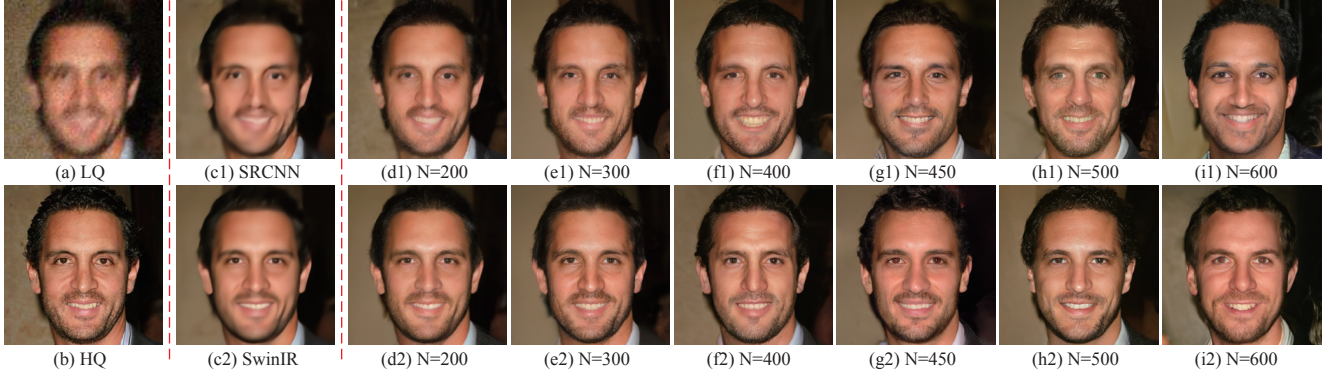


Figure 5. An example restored by *DiffFace* under different settings of the starting timestep N and the diffused estimator $f(\cdot; w)$. (a) LQ image, (b) HQ image, (c1)-(c2) restored results by SRCNN and SwinIR, (d1)-(i1) restored results by *DiffFace* that takes SRCNN as a diffused estimator, (d2)-(i2) restored results by *DiffFace* that takes SwinIR as a diffused estimator.

Attributed to such an error contraction, our method has a greater error tolerance to the diffused estimator. Hence, $f(\cdot; w)$ can be simply trained with L_2 loss on some synthetic data in this work. This unique flexibility bypasses the sophisticated training process compared with most recent methods [14, 24, 45]. What is more, this capability of compressing errors intuitively improves the robustness of our method, especially when dealing with severe and complex degradations.

- **Diffusion Prior.** After obtaining the diffused x_N via Eq. (10), our method gradually generates the desirable HQ result by sampling recursively from $p_\theta(x_{t-1}|x_t)$ starting from $t = N$ and ending at $t = 1$. Through this sampling procedure, we effectively leverage the rich image priors and powerful generation capability of the pre-trained diffusion model to help the restoration task. Unlike existing methods, since the diffusion model is completely trained on the HQ images in an unsupervised manner, it thus reduces the dependence of our method on the manually synthesized training data, of which the distribution may deviate from the true degradation.

These two intrinsic properties are mainly delivered by the constructed posterior in Eq. (5), which is the core formulation of our method. Such a posterior is specifically designed for BFR to mitigate the robustness issue caused by complicated degradations. Therefore, our proposed method indeed renders a new simple yet robust learning paradigm for BFR, rather than a straightforward application of diffusion model in this problem.

5. Model Analysis

In this section, we analyze the influence of the starting timestep N and the diffused estimator $f(\cdot; w)$ to our model. We consider two classical network architectures as the backbone for $f(\cdot; w)$, i.e., SRCNN [9] and SwinIR [26]. In the rest of this paper, we briefly denote the proposed

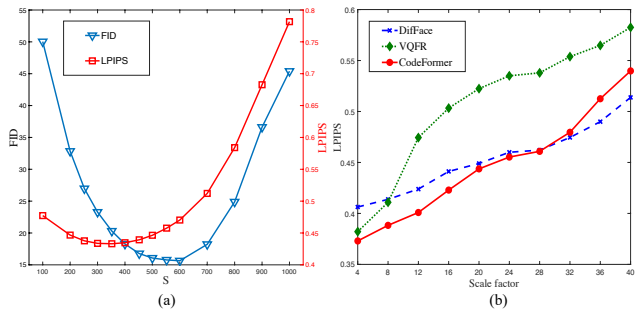


Figure 6. From left to right: (a) FID and LPIPS with respect to the starting timestep N on the validation dataset, (b) LPIPS with respect to the downsampling factor, namely s in Eq. (11), on the testing dataset.

method as *DiffFace* for convenience of presentation.

Training Settings. We train the diffused estimator $f(\cdot; w)$ on the FFHQ dataset [21] that contains 70000 HQ face images. We firstly resize the HQ images into a resolution of 512×512 , and then synthesize the LQ images following a typical degradation model used in recent literature [45]:

$$\mathbf{y} = \left\{ [(x * \mathbf{k}_l) \downarrow_s + \mathbf{n}_\sigma]_{\text{JPEG}_q} \right\} \uparrow_s, \quad (11)$$

where \mathbf{y} and \mathbf{x} are the LQ and HQ image, \mathbf{k}_l is the Gaussian kernel with kernel width l , \mathbf{n}_σ is Gaussian noise with standard deviation σ , $*$ is 2D convolutional operator, \downarrow_s and \uparrow_s are the Bicubic downsampling or upsampling operators with scale s , and $[\cdot]_{\text{JPEG}_q}$ represents the JPEG compression process with quality factor q . And the hyper-parameters l , s , σ , and q are uniformly sampled from $[0.1, 15]$, $[0.8, 32]$, $[0, 20]$, and $[30, 100]$ respectively. To evaluate the performances of *DiffFace* under different settings for N and $f(\cdot; w)$, we selected 4000 HQ images from CelebA-HQ [20] and generated the LQ images via Eq. (11) as our validation dataset.

We adopt the Adam [22] algorithm to optimize the network parameters w under L_2 loss. The batch size is set as

Table 1. Quantitative comparisons of different methods on CelebA-Test. The best and second best results are highlighted in **bold** and underline, respectively.

Metrics	Methods							
	DFDNet [24]	PULSE [30]	PSFRGAN [4]	GLEAN [3]	GFPGAN [45]	VQFR [14]	CodeFormer [52]	<i>DiffFace</i>
PSNR \uparrow	22.39	21.59	21.80	22.34	21.25	21.11	<u>22.60</u>	23.30
SSIM \uparrow	0.627	<u>0.675</u>	0.615	0.648	0.615	0.570	0.646	0.694
LPIPS \downarrow	0.582	0.519	0.522	0.502	0.532	0.506	0.440	<u>0.453</u>
FID \downarrow	83.96	50.54	67.13	82.34	68.91	61.55	<u>26.67</u>	20.72
IDS \downarrow	86.65	76.70	73.84	73.26	73.49	72.23	65.02	<u>66.17</u>

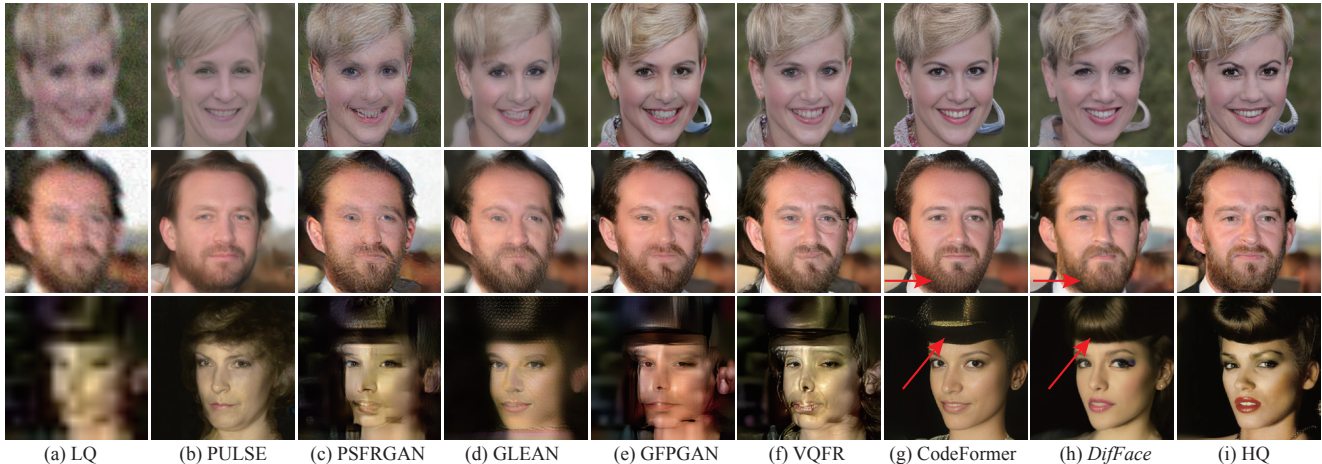


Figure 7. Visual comparisons of different methods on the synthetic dataset CelebA-Test.

16, and other settings of Adam follow the default configurations of Pytorch [34]. We train the model for 600k iterations, and the learning rate is decayed gradually from $1e-4$ to $1e-6$ with the cosine annealing schedule [27]. The leveraged diffusion model was trained on the FFHQ [20] dataset based on the official code¹ of [7]. It contains 1,000 discrete diffusion steps, and is accelerated to 250 steps using the technique in [32] when applied in *DiffFace*.

Starting Timestep. In Fig. 5, we show some restored results by *DiffFace* under different settings for the starting timesteps N . The results show that one can make a trade-off between realism and fidelity through different choices of N . In particular, if we set a larger N , the restored results would appear more realistic but with lower fidelity in comparison to the ground truth HQ images. The phenomenon is reflected by the average FID [15] and LPIPS [51] scores with respect to N in Fig. 6 (a). The proposed *DiffFace* performs very well in the range of [400, 450], and we thus set N as 400 throughout the whole experiments in this work. In practice, we speed up the inference four times following [32], and thus sample 100 steps for each testing image.

Diffused Estimator. Figure 5 displays an example restored by *DiffFace*, which either takes SRCNN [9] or SwinIR [26] as the diffused estimator $f(\cdot; w)$. More details and comparisons on these two backbones are provided in Appendix B. Even with the simplest SRCNN that only contains several

plain convolutional layers, *DiffFace* is able to restore a plausible HQ image. Using a more elaborated architecture like SwinIR results in more apparent details (e.g., hairs). The results suggest the versatility of *DiffFace* in the choices of the diffused estimators. In the following experiments, we use SwinIR as our diffused estimator.

6. Experimental Results

In this section, we conducted extensive experiments to verify the effectiveness of *DiffFace* on both synthetic and real-world datasets. The training follows the settings detailed in Sec. 5.

6.1. Evaluation Setting

Testing Datasets. We evaluate *DiffFace* on one synthetic dataset and three real-world datasets. The synthetic dataset, denoted as CelebA-Test, contains 4000 HQ images from CelebA-HQ [20], and the corresponding LQ images are synthesized via Eq. (11). The specific settings on the hyperparameters of the degradation can be found in Appendix A. As for the real-world datasets, we consider three typical ones with different degrees of degradation, namely LFW-Test, WebPhoto-Test [45], and WIDER-Test [52]. LFW-Test consists of 1711 mildly degraded face images in the wild, which contains one image for each person in LFW dataset [18]. WebPhoto-Test is made up of 407 face images crawled from the internet. Some of them are old photos

¹<https://github.com/openai/guided-diffusion>

Table 2. FID scores of different methods on three real-world testing datasets. The best and second best results are highlighted in **bold** and underline, respectively.

Datasets	# Images	Methods							
		DFDNet	PULSE	PSFRGAN	GLEAN	GFPGAN	VQFR	CodeFormer	<i>DifFace</i>
WIDER-Test	970	58.23	69.55	49.85	70.12	39.76	44.54	<u>39.21</u>	37.49
LFW-Test	1711	59.83	65.17	49.80	<u>46.39</u>	50.13	50.88	52.42	45.23
WebPhoto-Test	407	92.82	86.40	85.45	94.34	87.86	75.46	<u>83.70</u>	85.52

with severe degradation. WIDER-Test selects 970 face images with very heavy degradations from the WIDER Face dataset [49], thus is suitable to test the robustness of different methods under severe degradations.

Comparison Methods. We compare *DifFace* with seven recent BFR methods, including DFDNet [24], PULSE [30], PSFRGAN [4], GLEAN [3], GFPGAN [45], VQFR [14], and CodeFormer [52].

6.2. Evaluation on Synthetic Data

To evaluate different methods comprehensively, we adopt five quantitative metrics, namely PSNR, SSIM [46], LPIPS [51], FID [15], and Identity Score (IDS). Specifically, LPIPS is a learned perceptual similarity metric calculated based on deep features of VGG [41]. IDS is the embedding angle of ArcFace [6] between two images, mainly reflecting identity preservation. FID measures the KL divergence between the feature distributions (assumed as Gaussian) of the restored images and the ground truth images.

We summarize the comparative results on CelebA-Test in Table 1. The proposed *DifFace* achieves the best or second-best performance across all five metrics, indicating its effectiveness and superiority in the task of BFR. To further verify the robustness of *DifFace*, we compare it with recent state-of-the-art methods, namely CodeFormer and VQFR, using LPIPS under different degrees of degradation in Fig. 6 (b). We generate different degrees of degradation by increasing the scale factors from 4 to 40 with step 4 gradually, to the images in CelebA-Test. A total of 400 image pairs are generated for each scale. Figure 6 (b) records the averaged performance of different methods over these 400 images with respect to different downsampling scale factors. While *DifFace* is slightly inferior to CodeFormer and VQFR under small scale factors (mild degradations), its performance drops more gracefully and surpasses them in the cases of larger factors (severe degradations). These results substantiate the robustness of our *DifFace* in the scenarios with very severe degradations and is consistent with the analysis in Sec. 4.3.

For visualization, three typical examples of the CelebA-Test are shown in Fig. 7. In the first example with mild degradation, most of the methods are able to restore a realistic-looking image. PULSE produces a plausible face but fails to preserve the identity since its optimization cannot find the correct latent code through GAN inversion.

Table 3. Performance comparisons of *DifFace* under different acceleration settings. “*Dif(A/B)*” means that the whole reverse process of the pretrained diffusion model contains A sampling steps, and the starting timesteps N in *DifFace* is set as B. Besides, we also report the comparisons on the model size, i.e., the number of parameters (in megas), and the runtime (in seconds). It should be noted that, as for *DifFace*, the number of parameters of the pretrained diffusion model is also included and marked by “gray”.

Methods	PSNR	SSIM	LPIPS	FID	Runtime	# Params
<i>Dif(500/200)</i>	23.27	0.686	0.457	20.30	8.58	15.79 +159.59
<i>Dif(250/100)</i>	23.30	0.694	0.453	20.72	4.32	
<i>Dif(100/40)</i>	23.29	0.698	0.453	23.63	1.77	
<i>Dif(50/20)</i>	23.20	0.701	0.459	27.40	0.92	
<i>Dif(20/8)</i>	22.20	0.662	0.515	31.42	0.41	
CodeFormer	22.60	0.646	0.440	26.67	0.08	94.11
DFDNet	22.39	0.627	0.582	83.96	1.40	240.11
PULSE	21.59	0.675	0.519	50.54	3.93	24.11

In the second and third examples that exhibit more severe degradation, only CodeFormer and *DifFace* can handle such cases and return satisfactory face images. However, the results of CodeFormer still contain some slight artifacts in the areas of whiskers and hairs (marked by red arrows in Fig. 7). Compared with CodeFormer, *DifFace* performs more stably under this challenging degradation setting. Such robustness complies with our observation in Fig. 6 (b).

6.3. Evaluation on Real-world Data

In the experiments on real-world datasets, we mainly adopt FID as the quantitative metric since the ground truths are inaccessible. We first estimate the feature statistics on the restored images and the HQ images in FFHQ [21] dataset, respectively, and then calculate the KL divergence as FID. We attempted other non-reference metrics, such as NIQE [31], NRQM [28], and PI [2]. These metrics are not adopted here as we empirically found that they behave unusually pessimistic for diffusion-based methods. For completeness, we provide the experimental results on non-reference metrics in Appendix E.

The comparative results are summarized in Table 2. We can observe that *DifFace* achieves the best performance on both WIDER-Test and LFW-Test. On the WebPhoto-Test, it also surpasses most recent BFR methods. It should be noted that the FID values on WebPhoto-Test may not be representative as this dataset contains too few images (total 407) to estimate the feature distribution of the restored images. To

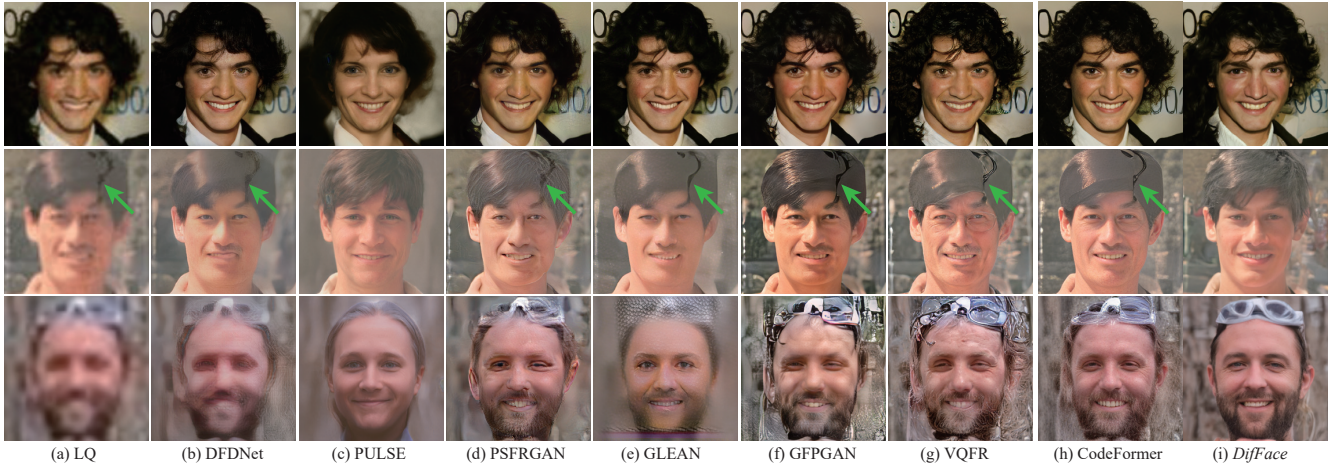


Figure 8. Visual comparisons of different methods on the real-world examples from LFW-Test (first row), WebPhoto-Test (second row), and WIDER-Test (third row).

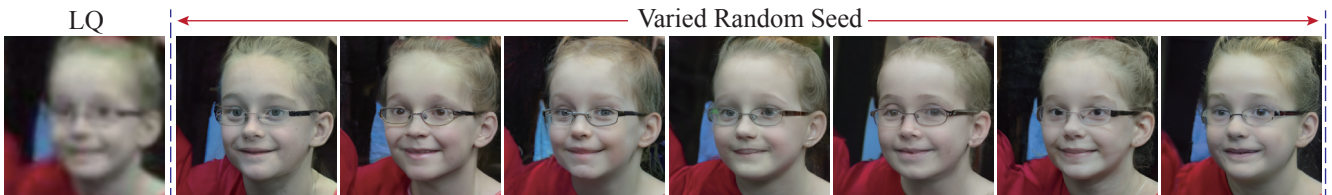


Figure 9. Unlike most existing BFR methods, *DifFace* can generate multiple diverse and plausible results given a LQ image, by setting different random seeds for the diffusion model. This example is extracted from real-world dataset WIDER-Test.

supplement the analysis, we show three typical examples of these datasets in Fig. 8, and more visual results are given in Fig. 14 of Appendix. It is again observed that *DifFace* provides better results, especially in the second and third examples with severe unknown degradations.

Most existing BFR methods produce only one HQ image for each LQ input, although there may be many reasonable possibilities. This is because they only learn a deterministic mapping between the LQ and HQ images. It is interesting to note that *DifFace*, as shown in Fig. 9, is capable of producing multiple diverse and plausible HQ solutions for any given LQ image by setting different random seeds for the pretrained diffusion model. More results are shown in Fig. 12 of Appendix. This “pluralistic” property is favorable in BFR, as there exist many different HQ images that can generate the same LQ counterpart.

6.4. Limitation

Despite the good performance of *DifFace*, the inference efficiency of our method is limited by the iterative sampling process inherited from the diffusion model. In this paper, we mainly report the results of *DifFace* by setting the starting timestep to be 100. To more comprehensively evaluate its efficiency, we list the performances of *DifFace* on CelebA-Test under different acceleration settings in Table 3. We can see that it is possible to reduce the sampling

process to 20 steps without evident performance drop. Under this setting, *DifFace* is still comparable to CodeFormer. This cuts the running time to 0.92s, lying between DFDNet and CodeFormer. In future work, we will explore more advanced accelerated techniques to further improve its inference speed. As for the model size, the diffused estimator and the pretrained diffusion model in *DifFace* contains 15.79M and 159.59M parameters respectively. This is also comparable to DFDNet and CodeFormer.

7. Conclusion

We have proposed a new BFR method called *DifFace* in this work. *DifFace* is appealing as it only relies on a restoration backbone that is trained with L_2 loss. This vastly simplifies the complicated training objectives in most current approaches. Importantly, we have proposed a posterior distribution that is well-suited for BFR. It consists of a transition kernel and a Markov chain partially borrowed from a pre-trained diffusion model. The former acts as an error compressor, and thus makes our method more robust to severe degradations. The latter effectively leverages the powerful diffusion model to facilitate BFR. Extensive experiments have demonstrated the effectiveness and robustness of our method both on synthetic and real-world datasets. We hope that this work could inspire more robust diffusion-based restoration methods in the future.

References

- [1] Christopher M Bishop and Nasser M Nasrabadi. *Pattern recognition and machine learning*, volume 4. Springer, 2006. 4
- [2] Yochai Blau, Roey Mechrez, Radu Timofte, Tomer Michaeli, and Lihi Zelnik-Manor. The 2018 PIRM challenge on perceptual image super-resolution. In *Proceedings of the European Conference on Computer Vision (ECCV) Workshops*, pages 0–0, 2018. 7, 14
- [3] Kelvin CK Chan, Xintao Wang, Xiangyu Xu, Jinwei Gu, and Chen Change Loy. GLEAN: generative latent bank for large-factor image super-resolution. *IEEE Transactions on Pattern Analysis and Machine Intelligence (TPAMI)*, 2022. 1, 2, 3, 6, 7
- [4] Chaofeng Chen, Xiaoming Li, Lingbo Yang, Xianhui Lin, Lei Zhang, and Kwan-Yee K Wong. Progressive semantic-aware style transformation for blind face restoration. In *Proceedings of the IEEE/CVF Conference on Computer Vision and Pattern Recognition (CVPR)*, pages 11896–11905, 2021. 2, 4, 6, 7
- [5] Yu Chen, Ying Tai, Xiaoming Liu, Chunhua Shen, and Jian Yang. Fsrnet: End-to-end learning face super-resolution with facial priors. In *Proceedings of the IEEE/CVF Conference on Computer Vision and Pattern Recognition (CVPR)*, pages 2492–2501, 2018. 1, 2
- [6] Jiankang Deng, Jia Guo, Niannan Xue, and Stefanos Zafeiriou. ArcFace: additive angular margin loss for deep face recognition. In *Proceedings of the IEEE/CVF Conference on Computer Vision and Pattern Recognition (CVPR)*, pages 4690–4699, 2019. 7
- [7] Prafulla Dhariwal and Alexander Nichol. Diffusion models beat GANs on image synthesis. *Advances in Neural Information Processing Systems (NeurIPS)*, 34:8780–8794, 2021. 1, 3, 6, 15
- [8] Berk Dogan, Shuhang Gu, and Radu Timofte. Exemplar guided face image super-resolution without facial landmarks. In *Proceedings of the IEEE/CVF Conference on Computer Vision and Pattern Recognition (CVPR) Workshops*, pages 0–0, 2019. 2
- [9] Chao Dong, Chen Change Loy, Kaiming He, and Xiaoou Tang. Image super-resolution using deep convolutional networks. *IEEE Transactions on Pattern Analysis and Machine Intelligence (TPAMI)*, 38(2):295–307, 2015. 5, 6, 12
- [10] Patrick Esser, Robin Rombach, and Bjorn Ommer. Taming transformers for high-resolution image synthesis. In *Proceedings of the IEEE/CVF Conference on Computer Vision and Pattern Recognition (CVPR)*, pages 12873–12883, 2021. 3, 14
- [11] Lu Feihong, Chen Hang, Li Kang, Deng Qiliang, Zhao jian, Zhang Kaipeng, and Han Hong*. Toward high-quality face-mask occluded restoration. *ACM Transactions on Multimedia Computing, Communications, and Applications (TOMM)*, 2022. 1
- [12] Ian Goodfellow, Jean Pouget-Abadie, Mehdi Mirza, Bing Xu, David Warde-Farley, Sherjil Ozair, Aaron Courville, and Yoshua Bengio. Generative adversarial nets. *Advances in Neural Information Processing Systems (NeurIPS)*, 27, 2014. 1
- [13] Jinjin Gu, Yujun Shen, and Bolei Zhou. Image processing using multi-code GAN prior. In *Proceedings of the IEEE/CVF Conference on Computer Vision and Pattern Recognition (CVPR)*, pages 3012–3021, 2020. 3
- [14] Yuchao Gu, Xintao Wang, Liangbin Xie, Chao Dong, Gen Li, Ying Shan, and Ming-Ming Cheng. VQFR: blind face restoration with vector-quantized dictionary and parallel decoder. In *Proceedings of the European Conference on Computer Vision (ECCV)*, 2022. 1, 2, 3, 5, 6, 7
- [15] Martin Heusel, Hubert Ramsauer, Thomas Unterthiner, Bernhard Nessler, and Sepp Hochreiter. GANs trained by a two time-scale update rule converge to a local nash equilibrium. *Advances in Neural Information Processing Systems (NeurIPS)*, 30, 2017. 6, 7
- [16] Jonathan Ho, Ajay Jain, and Pieter Abbeel. Denoising diffusion probabilistic models. *Advances in Neural Information Processing Systems (NeurIPS)*, 33:6840–6851, 2020. 2
- [17] Xiaobin Hu, Wenqi Ren, John LaMaster, Xiaochun Cao, Xiaoming Li, Zechao Li, Bjoern Menze, and Wei Liu. Face super-resolution guided by 3D facial priors. In *Proceedings of the European Conference on Computer Vision (ECCV)*, pages 763–780. Springer, 2020. 2
- [18] Gary B Huang, Marwan Mattar, Tamara Berg, and Eric Learned-Miller. Labeled faces in the wild: A database for studying face recognition in unconstrained environments. In *Workshop on faces in 'Real-Life' Images: detection, alignment, and recognition*, 2008. 6
- [19] Justin Johnson, Alexandre Alahi, and Li Fei-Fei. Perceptual losses for real-time style transfer and super-resolution. In *Proceedings of the European Conference on Computer Vision (ECCV)*, pages 694–711. Springer, 2016. 1
- [20] Tero Karras, Timo Aila, Samuli Laine, and Jaakko Lehtinen. Progressive growing of GANs for improved quality, stability, and variation. In *Proceedings of the International Conference on Learning Representations (ICLR)*, 2018. 5, 6, 12, 13
- [21] Tero Karras, Samuli Laine, and Timo Aila. A style-based generator architecture for generative adversarial networks. In *Proceedings of the IEEE/CVF Conference on Computer Vision and Pattern Recognition (CVPR)*, pages 4401–4410, 2019. 3, 5, 7
- [22] Diederik P Kingma and Jimmy Ba. Adam: A method for stochastic optimization. In *Proceedings of the International Conference on Learning Representations (ICLR)*, 2015. 5
- [23] Haoying Li, Yifan Yang, Meng Chang, Shiqi Chen, Huajun Feng, Zhihai Xu, Qi Li, and Yueting Chen. SRDiff: single image super-resolution with diffusion probabilistic models. *Neurocomputing*, 479:47–59, 2022. 3
- [24] Xiaoming Li, Chaofeng Chen, Shangchen Zhou, Xianhui Lin, Wangmeng Zuo, and Lei Zhang. Blind face restoration via deep multi-scale component dictionaries. In *Proceedings of the European Conference on Computer Vision (ECCV)*, pages 399–415. Springer, 2020. 1, 2, 3, 5, 6, 7
- [25] Xiaoming Li, Ming Liu, Yuting Ye, Wangmeng Zuo, Liang Lin, and Ruigang Yang. Learning warped guidance for blind

- face restoration. In *Proceedings of the European conference on computer vision (ECCV)*, pages 272–289, 2018. [2](#)
- [26] Jingyun Liang, Jiezhong Cao, Guolei Sun, Kai Zhang, Luc Van Gool, and Radu Timofte. SwinIR: image restoration using swin transformer. In *Proceedings of the IEEE/CVF International Conference on Computer Vision (ICCV) Workshops*, pages 1833–1844, 2021. [5](#), [6](#), [12](#)
- [27] Ilya Loshchilov and Frank Hutter. SGDR: stochastic gradient descent with warm restarts. In *Proceedings of the International Conference on Learning Representations (ICLR)*. OpenReview.net, 2017. [6](#)
- [28] Chao Ma, Chih-Yuan Yang, Xiaokang Yang, and Ming-Hsuan Yang. Learning a no-reference quality metric for single-image super-resolution. *Computer Vision and Image Understanding*, 158:1–16, 2017. [7](#), [14](#)
- [29] Kangfu Mei and Vishal M. Patel. LTT-GAN: looking through turbulence by inverting gans. *CoRR*, abs/2112.02379, 2021. [14](#)
- [30] Sachit Menon, Alexandru Damian, Shijia Hu, Nikhil Ravi, and Cynthia Rudin. PULSE: self-supervised photo upsampling via latent space exploration of generative models. In *Proceedings of the IEEE/CVF Conference on Computer Vision and Pattern Recognition (CVPR)*, pages 2437–2445, 2020. [3](#), [6](#), [7](#)
- [31] Anish Mittal, Rajiv Soundararajan, and Alan C Bovik. Making a “completely blind” image quality analyzer. *IEEE Signal Processing Letters*, 20(3):209–212, 2012. [7](#), [14](#)
- [32] Alexander Quinn Nichol and Prafulla Dhariwal. Improved denoising diffusion probabilistic models. In *Proceedings of the International Conference on Machine Learning (ICML)*, pages 8162–8171. PMLR, 2021. [6](#)
- [33] Xingang Pan, Xiaohang Zhan, Bo Dai, Dahua Lin, Chen Change Loy, and Ping Luo. Exploiting deep generative prior for versatile image restoration and manipulation. *IEEE Transactions on Pattern Analysis and Machine Intelligence (TPAMI)*, 2021. [1](#), [3](#)
- [34] Adam Paszke, Sam Gross, Francisco Massa, Adam Lerer, James Bradbury, Gregory Chanan, Trevor Killeen, Zeming Lin, Natalia Gimelshein, Luca Antiga, et al. PyTorch: an imperative style, high-performance deep learning library. *Advances in Neural Information Processing Systems (NeurIPS)*, 32, 2019. [6](#)
- [35] Wenqi Ren, Jiaolong Yang, Senyou Deng, David Wipf, Xiaochun Cao, and Xin Tong. Face video deblurring using 3D facial priors. In *Proceedings of the IEEE/CVF International Conference on Computer Vision (ICCV)*, pages 9388–9397, 2019. [2](#)
- [36] Robin Rombach, Andreas Blattmann, Dominik Lorenz, Patrick Esser, and Björn Ommer. High-resolution image synthesis with latent diffusion models. In *Proceedings of the IEEE/CVF Conference on Computer Vision and Pattern Recognition (CVPR)*, pages 10684–10695, 2022. [3](#), [14](#)
- [37] Chitwan Saharia, William Chan, Huiwen Chang, Chris Lee, Jonathan Ho, Tim Salimans, David Fleet, and Mohammad Norouzi. Palette: Image-to-image diffusion models. In *Proceedings of the ACM SIGGRAPH Conference*, pages 1–10, 2022. [12](#)
- [38] Chitwan Saharia, Jonathan Ho, William Chan, Tim Salimans, David J Fleet, and Mohammad Norouzi. Image super-resolution via iterative refinement. *IEEE Transactions on Pattern Analysis and Machine Intelligence (TPAMI)*, 2022. [2](#), [3](#), [12](#)
- [39] Ziyi Shen, Wei-Sheng Lai, Tingfa Xu, Jan Kautz, and Ming-Hsuan Yang. Deep semantic face deblurring. In *Proceedings of the IEEE Conference on Computer Vision and Pattern Recognition (CVPR)*, pages 8260–8269, 2018. [2](#)
- [40] Wenzhe Shi, Jose Caballero, Ferenc Huszár, Johannes Totz, Andrew P Aitken, Rob Bishop, Daniel Rueckert, and Zehan Wang. Real-time single image and video super-resolution using an efficient sub-pixel convolutional neural network. In *Proceedings of the IEEE Conference on Computer Vision and Pattern Recognition (CVPR)*, pages 1874–1883, 2016. [12](#)
- [41] Karen Simonyan and Andrew Zisserman. Very deep convolutional networks for large-scale image recognition. In Yoshua Bengio and Yann LeCun, editors, *Proceedings of the International Conference on Learning Representations (ICLR)*, 2015. [7](#)
- [42] Jascha Sohl-Dickstein, Eric Weiss, Niru Maheswaranathan, and Surya Ganguli. Deep unsupervised learning using nonequilibrium thermodynamics. In *Proceedings of the International Conference on Machine Learning (ICML)*, pages 2256–2265. PMLR, 2015. [1](#), [3](#)
- [43] Yang Song, Jascha Sohl-Dickstein, Diederik P Kingma, Abhishek Kumar, Stefano Ermon, and Ben Poole. Score-based generative modeling through stochastic differential equations. In *Proceedings of the International Conference on Learning Representations (ICLR)*, 2020. [12](#), [15](#)
- [44] Xiaoguang Tu, Jian Zhao, Qiankun Liu, Wenjie Ai, Guodong Guo, Zhifeng Li, Wei Liu, and Jiashi Feng. Joint face image restoration and frontalization for recognition. *IEEE Transactions on Circuits and Systems for Video Technology (TCSVT)*, 32(3):1285–1298, 2021. [1](#)
- [45] Xintao Wang, Yu Li, Honglun Zhang, and Ying Shan. Towards real-world blind face restoration with generative facial prior. In *Proceedings of the IEEE/CVF Conference on Computer Vision and Pattern Recognition (CVPR)*, pages 9168–9178, 2021. [1](#), [2](#), [3](#), [4](#), [5](#), [6](#), [7](#)
- [46] Zhou Wang, Alan C Bovik, Hamid R Sheikh, and Eero P Simoncelli. Image quality assessment: from error visibility to structural similarity. *IEEE Transactions on Image Processing (TIP)*, 13(4):600–612, 2004. [7](#)
- [47] Zhouxia Wang, Jiawei Zhang, Runjian Chen, Wenping Wang, and Ping Luo. RestoreFormer: high-quality blind face restoration from undegraded key-value pairs. In *Proceedings of the IEEE/CVF Conference on Computer Vision and Pattern Recognition (CVPR)*, pages 17512–17521, 2022. [3](#)
- [48] Weihao Xia, Yulun Zhang, Yujiu Yang, Jing-Hao Xue, Bolei Zhou, and Ming-Hsuan Yang. GAN inversion: A survey. *IEEE Transactions on Pattern Analysis and Machine Intelligence (TPAMI)*, 2022. [3](#)
- [49] Shuo Yang, Ping Luo, Chen-Change Loy, and Xiaoou Tang. Wider face: A face detection benchmark. In *Proceedings of the IEEE Conference on Computer Vision and Pattern Recognition (CVPR)*, pages 5525–5533, 2016. [7](#)

- [50] Tao Yang, Peiran Ren, Xuansong Xie, and Lei Zhang. GAN prior embedded network for blind face restoration in the wild. In *Proceedings of the IEEE/CVF Conference on Computer Vision and Pattern Recognition (CVPR)*, pages 672–681, 2021. [1](#), [3](#), [4](#)
- [51] Richard Zhang, Phillip Isola, Alexei A Efros, Eli Shechtman, and Oliver Wang. The unreasonable effectiveness of deep features as a perceptual metric. In *Proceedings of the IEEE/CVF Conference on Computer Vision and Pattern Recognition (CVPR)*, pages 586–595, 2018. [1](#), [6](#), [7](#)
- [52] Shangchen Zhou, Kelvin C. K. Chan, Chongyi Li, and Chen Change Loy. Towards robust blind face restoration with codebook lookup transformer. *Advances in Neural Information Processing Systems (NeurIPS)*, 2022. [1](#), [2](#), [3](#), [6](#), [7](#)
- [53] Feida Zhu, Junwei Zhu, Wenqing Chu, Xinyi Zhang, Xiaozhong Ji, Chengjie Wang, and Ying Tai. Blind face restoration via integrating face shape and generative priors. In *Proceedings of the IEEE/CVF Conference on Computer Vision and Pattern Recognition (CVPR)*, pages 7662–7671, 2022. [2](#)

A. Setup on Validation and Testing Datasets

In the main text, we synthesized one validation dataset and one testing dataset, each of which contains 4,000 HQ images randomly selected from CelebA-HQ [20]. The former is used to select a reasonable starting timestep N for *DiffFace*, and the latter to evaluate the performance of different methods. To synthesize the LQ images, we employ the degradation model of Eq. (11) in the main text with the hyper-parameter settings in Table 4. Note that l_x , l_y , and θ is used to control the generation of the blur kernel \mathbf{k} through a variance matrix defined as follows:

$$U = \begin{bmatrix} \cos \theta & -\sin \theta \\ \sin \theta & \cos \theta \end{bmatrix}, \quad \Lambda = \begin{bmatrix} l_x^2 & 0 \\ 0 & l_y^2 \end{bmatrix}, \quad \Sigma = U \Lambda U^T. \quad (12)$$

B. Diffused Estimator

B.1. Network Architectures

We consider two typical restoration backbones for the diffused estimator $f(\cdot; w)$, namely SRCNN [9] and SwinIR [26]. To apply them in our method, we slightly adjust their settings. The LQ/HQ image pairs in our method are both with size 512×512 , we add two (or three) PixelUnshuffle [40] layers with a downscale factor 2 to reduce the input size to 128×128 (or 64×64) for SRCNN (or SwinIR). After each PixelUnshuffle layers except the last one, one convolutional and LeakyReLU layers are followed to fuse the features. Similarly, two (or three) PixelShuffle [40] layers are also added to the tail of SRCNN (or SwinIR) to up-sample the size back to 512×512 .

As for SRCNN, we adopt nine convolutional layers with kernel size 5 between the PixelUnshuffle and PixelShuffle layers, and each convolutional layer has 64 channels. As for SwinIR, we follow the official settings² for real-world image super-resolution task with a scale factor 8.

B.2. Performance Comparison

To quantitatively evaluate these two restoration backbones and their influences to *DiffFace*, we conduct experiments on CelebA-Test and summarize the results in Table 5. We also provide some quantitative comparisons in Figure 10 on the real datasets LFW-Test (top row) and WIDER-Test (bottom row). The results offer a few observations as follows:

- Even though taking the simplest backbone SRCNN as our diffused estimator, *DiffFace* is still able to produce highly natural-looking results with realistic image details, such as hairs and stubbles. This delivers that the proposed *DiffFace* does not rely on specific designs on the diffused estimator.

²<https://github.com/JingyunLiang/SwinIR>

Table 4. Hyper-parameter settings of the degradation model on the validation and testing data sets. Note that l_x , l_y , and θ control the generation of the blur kernel \mathbf{k} through a covariance matrix defined in Eq. (12).

Hyper-parameters	range set
s	{4, 8, 16, 24, 32, 36, 40}
σ	{1, 5, 10, 15, 20}
q	{30, 40, 50, 60, 70}
l_x, l_y	{2, 4, 6, 8, 10, 12, 14}
θ	{0, 0.25 π , 0.5 π , 0.75 π }

- Owing to more advanced network architectures as well as more learnable parameters, SwinIR outperforms SRCNN in both qualitative and quantitative comparisons.
- When the starting timestep N gets larger, *DiffFace* is capable of achieving more realistic results. However, larger N will introduce more randomness and thus reduce the fidelity.

Based on these observations, we suggest taking SwinIR as the diffused estimator attributed to its superior performance. As for the starting timestep N , the proposed *DiffFace* performs stably and well when fixing it in the range [400, 450].

C. Bicubic Super-Resolution

Diffusion model can be used for image restoration by directly introducing the LQ image \mathbf{y}_0 as a condition to guide the generation of \mathbf{x}_0 [37, 38, 43], namely

$$p(\mathbf{x}_0 | \mathbf{y}_0) = \int p(\mathbf{x}_T) \prod_{t=1}^T p_\theta(\mathbf{x}_{t-1} | \mathbf{x}_t, \mathbf{y}_0) d\mathbf{x}_{1:T}, \quad (13)$$

where $p(\mathbf{x}_T) = N(\mathbf{x}_T | \mathbf{0}, \mathbf{I})$, $p_\theta(\mathbf{x}_{t-1} | \mathbf{x}_t, \mathbf{y}_0)$ is the learned transition kernel from \mathbf{x}_t to \mathbf{x}_{t-1} conditioned on \mathbf{y}_0 . To access such a transition kernel, an intuitive way is to re-train the diffusion model from scratch. Specifically, in each timestep t , \mathbf{x}_t and \mathbf{y}_0 are concatenated together as input to predict \mathbf{x}_{t-1} in training. Following this paradigm, SR3 [38] trained a diffusion model for image super-resolution based on bicubic degradation.

We omit the comparison against SR3 [38] in the main text as it can only deal with bicubic degradation. Here, we extend the proposed *DiffFace* to bicubic super-resolution and make a fair comparison with SR3. We do not make any changes apart from upsampling an LQ image with bicubic interpolation and feeding it into *DiffFace* to restore the high-resolution target. Although the degradation model we use (Eq. (11) of the maintext) does not contain the bicubic degradation, we do not retrain or finetune our diffused estimator on such degradation.

Since the code of SR3 is not released, we thus adopt an

Table 5. Quantitative comparisons of SRCNN, SwinIR and *DifFace* on CelebA-Test. “*DifFace*(X)” means that it takes the backbone “X” as the diffused estimator $f(\cdot; w)$. The parameters in “*DifFace*(X)” includes both of that in the backbone “X” and the pre-trained diffusion model (159.59M).

Methods	Metrics					
	PSNR \uparrow	SSIM \uparrow	LPIPS \downarrow	FID \downarrow	IDS \downarrow	# Parameters(M)
SRCNN	23.58	0.722	0.555	108.68	73.09	1.03
<i>DifFace</i> (SRCNN)	22.88	0.685	0.487	32.06	70.65	1.03+159.59
SwinIR	24.32	0.736	0.507	93.73	63.80	15.79
<i>DifFace</i> (SwinIR)	23.30	0.694	0.453	20.72	66.17	15.79+159.59

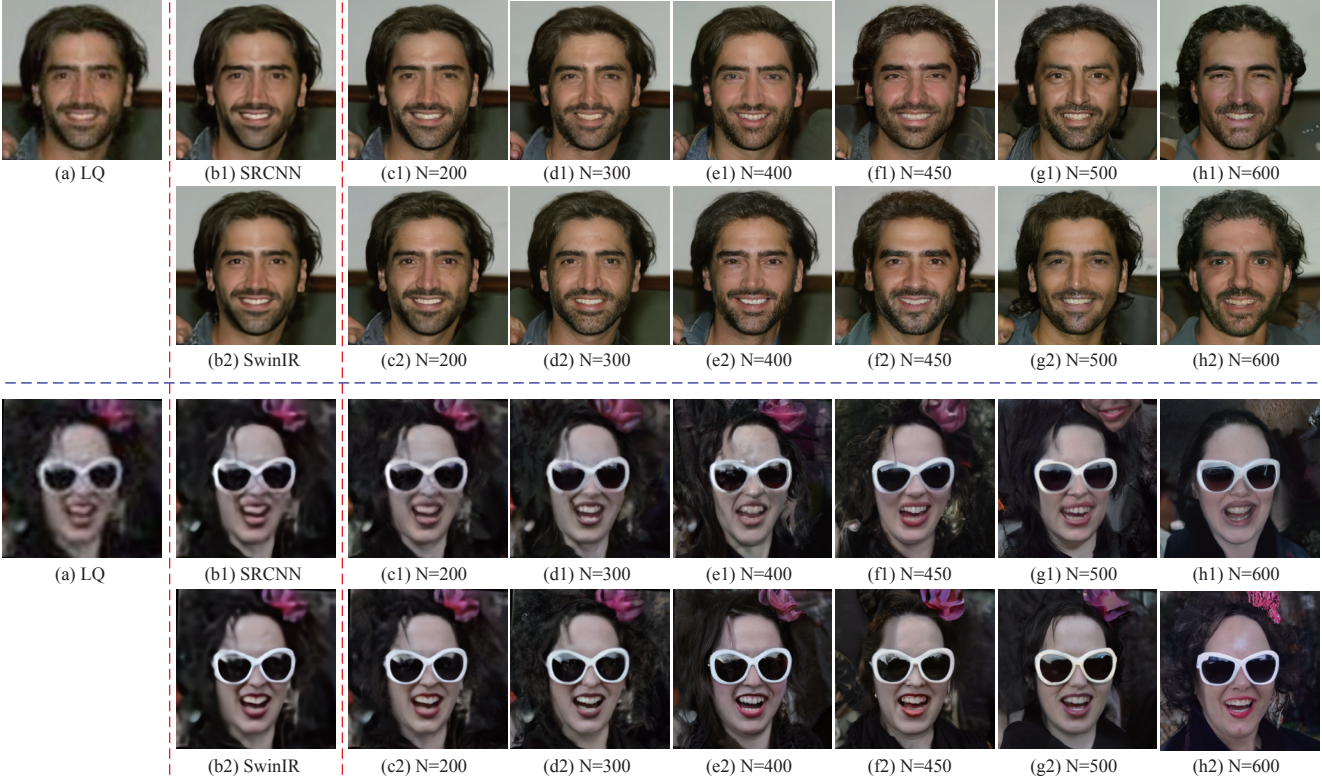


Figure 10. Qualitative comparisons of *DifFace* on LFW-Test (top row) and WIDER-Test (bottom row) under different settings for the starting timestep N and the diffused estimator $f(\cdot; w)$. (a) LQ image, (b1)-(b2) restored results by SRCNN and SwinIR, (c1)-(h1) restored results by *DifFace* that takes SRCNN as diffused estimator, (c2)-(h2) restored results by *DifFace* that takes SwinIR as diffused estimator.

Table 6. Quantitative results of SR3 and *DifFace* on bicubic face image super-resolution.

Methods	Scale factors	Metrics			
		PSNR \uparrow	SSIM \uparrow	LPIPS \downarrow	IDS \downarrow
SR3	x8	22.74	0.585	0.505	25.66
<i>DifFace</i>		27.24	0.754	0.375	38.89
SR3	x16	20.50	0.506	0.645	64.19
<i>DifFace</i>		25.03	0.712	0.412	51.36

unofficially re-implemented version³ instead. This model is specifically trained for 8x face image super-resolution from size 64×64 to 512×512 . To further evaluate the generaliza-

³<https://github.com/Janspiry/Image-Super-Resolution-via-Iterative-Refinement>

tion capability to different degradation, we also test its performance on the task of 16x super-resolution from 32×32 to 512×512 . As for the testing dataset, we randomly select 200 images from CelebA-HQ [20].

Table 6 lists the quantitative results of SR3 and *DifFace* on the task of bicubic super-resolution, and the corresponding visual comparisons are shown in Fig. 11. *DifFace* achieves better or at least comparable performance on 8x super-resolution, even though SR3 is specifically trained for this bicubic upsampling task. When generalized to 16x super-resolution, *DifFace* outperforms SR3 on both qualitative and quantitative comparisons, indicating the robustness of *DifFace* to unknown degradations. On the other hand, *DifFace* is more efficient than SR3, because SR3 has to pass through the whole reverse process of the diffusion model

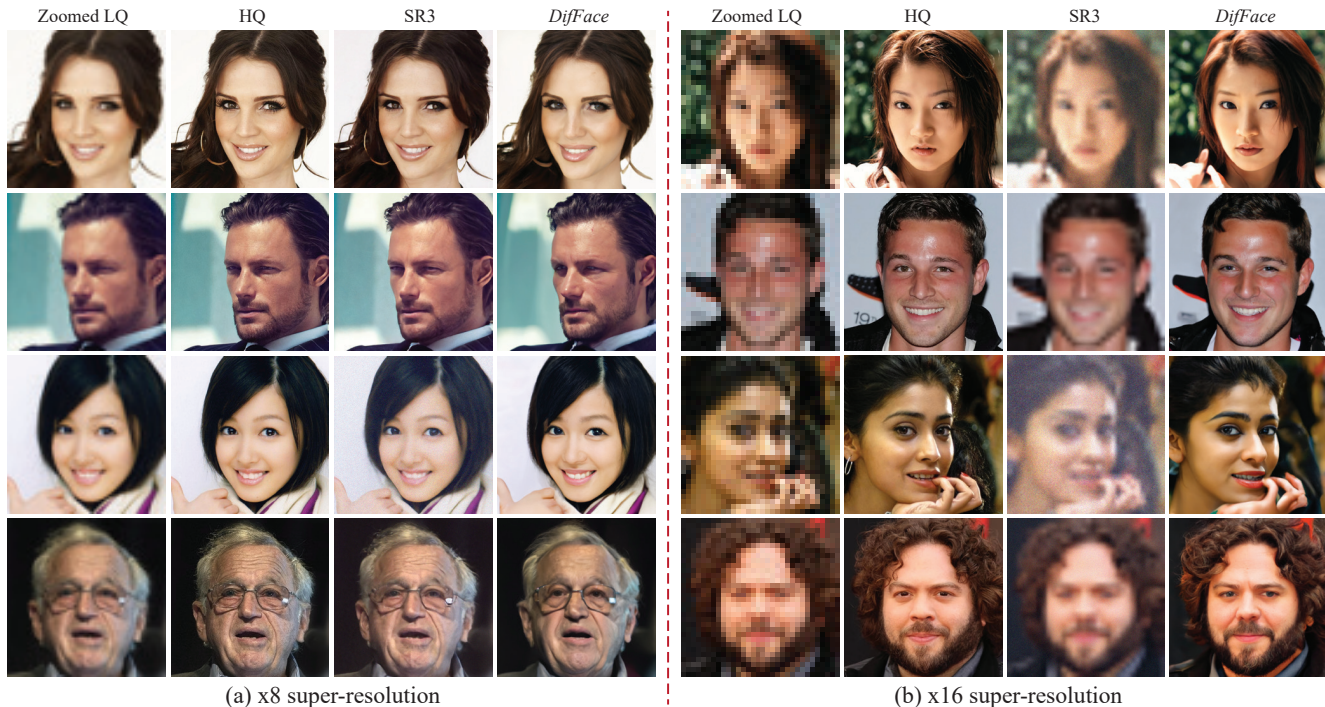


Figure 11. Visual comparisons of SR3 and *DiffFace* on 8x (left) and 16x (right) face image super-resolution.

while *DiffFace* starts from the intermediate state (i.e., x_N) of the reverse Markov chain.

Another popular diffusion based image super-resolution model is LDM [36]. It trains a diffusion model to approximate the conditional distribution in Eq. (13) in the latent space of VQGAN [10], which evidently accelerates its inference speed. Since LDM only releases a pretrained model trained on natural images, we thus cannot provide comparisons with it on the task of BFR.

D. Atmospheric Turbulence Restoration

In this section, we consider a more challenging degradation type, namely atmospheric turbulence. It causes geometric distortion and blur effects on the captured images, and negatively affects the face-related downstream tasks. Note that none of the *DiffFace* and the other comparison methods contains any atmospheric turbulence or similar degradation types. Hence, it is suitable to compare the robustness of different methods on such a degradation type.

It is difficult to collect a large real-world dataset degraded by atmospheric turbulence, since most of the relevant datasets are privately protected due to their military use. We cropped eight real-world image pairs from the manuscript of [29], and resize them to the resolution of 512. Each pair contains one image degraded by atmospheric turbulence and one corresponding reference image. We call this dataset as Turb8-Test in this work.

Figure 13 shows the qualitative comparison results of

different methods on Turb8-Test dataset. *DiffFace* is able to achieve photo-realistic results and evidently outperforms other methods in visual quality. In particular, the first three examples represent the same person but with large pose variations, *DiffFace* still performs well in this scenario. Unfortunately, *DiffFace* sometimes cannot preserve the identity very well when the input loses too much image information, e.g., the last example in Fig. 13. We leave this problem to future research.

E. Discussion on Non-Reference Metrics

In Sec.6.3, we evaluate the performance of different methods on real-world data using FID score. In this section, we further consider three commonly used non-reference metrics, namely NIQE [31], NRQM [28], and PI [2]. Table 7 summarizes the detailed comparisons on WIDER-Test. Despite the strong superiority of *DiffFace*, it shows a surprisingly weak performance against GAN based methods (e.g., VQFR, GFPGAN, and PSFRGAN) across these three non-reference metrics.

To explore the underlying reasons behind this phenomenon, we randomly generate 3,000 HQ face images using the pre-trained diffusion model, and then evaluate their image quality based on these non-reference metrics. The average results are denoted as “Diffusion” and marked by gray color in Table 7. One can regard this performance as the upper bound of our proposed *DiffFace*.

It is interesting to observe that even this upper bound is

Table 7. Non-reference metrics of different methods on the real-world dataset WIDER-Test. “Diffusion” denotes the average results on 3,000 images randomly generated by the pretrained diffusion model, which can be regarded as the upper bound of *DiffFace*.

Metrics	Methods								
	DFDNet	PULSE	PSFRGAN	GLEAN	GFPGAN	VQFR	CodeFormer	<i>DiffFace</i>	Diffusion
NIQE↓	5.67	5.27	3.89	5.13	3.81	3.02	4.12	4.24	4.11
NRQM↑	6.80	4.05	8.01	7.03	8.07	8.78	8.49	6.11	6.60
fPI↓	4.81	5.88	3.33	4.45	3.08	2.17	3.01	4.46	4.17

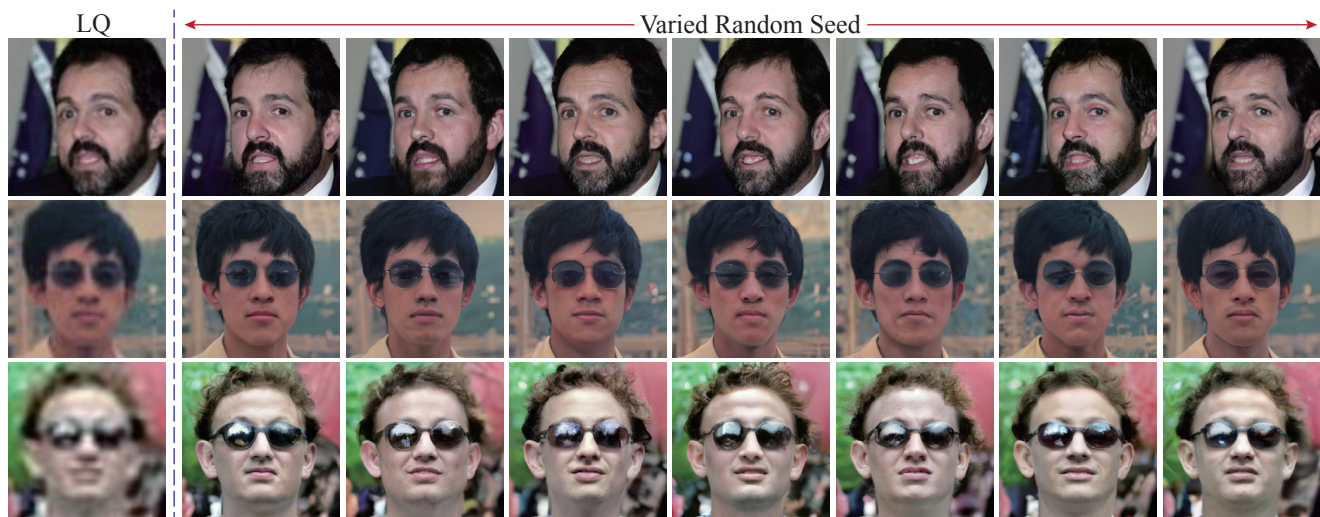


Figure 12. Three restoration examples of *DiffFace* on the real-world dataset WIDER-Test by setting different random seeds for the diffusion model.

inferior to GAN based restoration methods. Such a conclusion is unreasonably pessimistic considering the various positive results of diffusion models reported against GANs [7, 43]. More investigations are called to study this gap introduced by the aforementioned non-reference metrics.

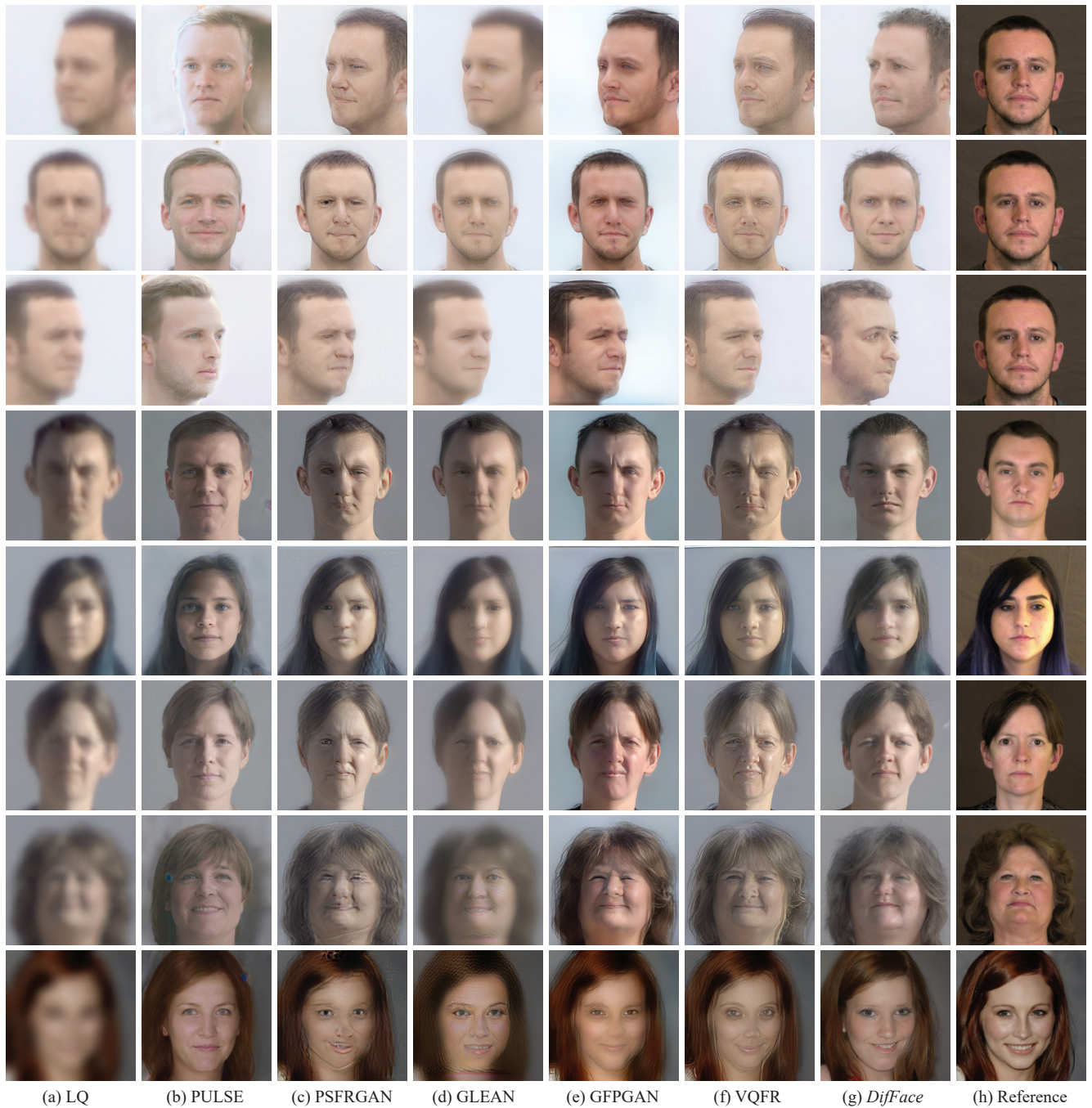


Figure 13. Qualitative comparisons of different methods on the real-world Turb8-Test dataset.



Figure 14. Visual comparisons of different method on three real-world datasets.